Journal of Combinatorial Mathematics
and Combinatorial Computing
www.combinatorialpress.com/jcmcc

$CoMoO_4$-coated Co_3O_4 hierarchical composite structures grown on nickel foam as ultra-high performance binder-free electrodes

Xuehu Wu[1, ✉]

[1] *School of Materials Science and Engineering, Guilin University of Electronic Science and Technology, Guilin, Guangxi, 541004, China*

ABSTRACT

In the realm of supercapacitor energy storage, multi-element transition metal-oxides with high theoretical specific-capacitance values have been extensively explored. However, their poor electrical conductivity and cycling stability limit their applications. In this study, $CoMoO_4$@Co_3O_4/NF was formed by loading Co_3O_4 on the nickel foam (NF) surface as a substrate by solvent co-precipitation method and annealing treatment first, and then growing $CoMoO_4$ on the surface of Co_3O_4 by hydrothermal reaction and calcination. Co_3O_4 nanosheets, which are derived from ZIF-67, offer more active sites and simpler ion/electron transport paths. The electrochemical characteristics of the composite electrode can be substantially boosted by the synergistic effect between Co_3O_4 as the inner layer and $CoMoO_4$ as the outer layer in the $CoMoO_4$@Co_3O_4/nickel foam hierarchical composite structural materials. When combined with activated carbon (AC) to form an asymmetric supercapacitor, it exhibits a capacitance normalized to unit area of 0.669 F cm2 at 1 mA cm2. Furthermore, the assembled asymmetric supercapacitor demonstrates an energy per unit volume of 209.29 mWh cm^{-2} at the current flux of 0.75 mW cm^{-2}, and upholds 89% of its Initial surface capacitance after 6000 cycles.

Keywords: Hierarchical composite, Cobalt-based metal oxide, Bimetallic oxide, Asymmetric supercapacitors

1. Introduction

Nickel foam refers to the porous structure material made of nickel material. In the preparation process, the nickel powder is sintered into spherical particles at high temperature by controlling the particle size of the nickel powder and adding a control agent, and then the spherical particles are expanded into a porous structure under a high temperature and high pressure hydrogen atmosphere,

✉ Corresponding author.
E-mail address: 18706706920@163.com (X. Wu).
Received 15 January 2024; Revised 20 February 2024; Accepted 30 November 2024; Published Online 16 April 2025.
DOI: 10.61091/jcmcc127b-476

finally forming a foamy nickel material [1-4]. Nickel foam is a new type of porous metal material with a wide range of applications, which has a low density and high specific surface area, and is widely used in catalysts, batteries, filters and other fields [5-7].

Adhesive-free electrodes are electrodes without any adhesive or glue between the electrodes and electrode leads and are connected by a special mechanical structure [8-9]. Compared with conventional adhesive electrodes, adhesive-free electrodes have the following advantages: easy to install: due to the absence of adhesives, adhesive-free electrodes are very simple to install, requiring only the insertion of the electrodes and wires into the electrode sockets. This makes the replacement and cleaning of adhesive-free electrodes very easy [10-13]. Better electrode connection: Traditional adhesive electrodes are prone to lose connection performance due to aging, contamination, and damage of the adhesive, whereas adhesive-free electrodes can maintain better connection performance through a special mechanical structure, which improves signal stability and accuracy [14-17]. Longer service life: Due to the absence of adhesive, the service life of adhesive-free electrodes is longer. Also, the mechanically connected structure of adhesive-free electrodes reduces the mechanical stress on the electrodes, which further extends the service life of the electrodes [18-21]. Adhesive-free electrodes are widely used in biomedical field, environmental monitoring field, energy field, etc [22].

In this work, $CoMoO_4@Co_3O_4$/NF hierarchical composite structural materials were prepared. Initially, Co_3O_4 was deposited on the surface of nickel foam through solvent co-precipitation and subsequent annealing. Then, $CoMoO_4$ was grown on the Co_3O_4 surface using a hydrothermal method followed by calcination. This unique composite material consists of Co_3O_4 nanosheets as the inner layer and $CoMoO_4$ nanorods as the outer layer. The sheet-like structure of Co_3O_4 provides favorable factors for the even dispersion and growth of $CoMoO_4$, causing the composite electrode having a larger high surface area and plentiful active sites. Taking advantage of these benefits, the $CoMoO_4@Co_3O_4$/NF hierarchical composite structure material demonstrates superior electrochemical performance and cycle durability.

2. Experimental

2.1. Preparation of Co_3O_4/NF

Firstly, 0.874 g of Co $(NO_3)_2 \cdot 6H_2O$, and 1.971 g of 2-Methylimidazole were respectively dissolved into 65 mL of de-ionized water. Then, the solutions were mixed quickly and agitated for three minutes. Then, the pretreated nickel foam (2 × 4 cm2) was inserted vertically into the mixed solution and kept standing for 4 hours at room temperature. Then, the nickel foam grown with ZIF-67 was taken out and dried under vacuum at 65 ℃ for 12.5 hours. Finally, anneal in air at 355 ℃ for 2 hours to obtain Co_3O_4/NF.

2.2. Synthesis of $CoMoO_4@Co_3O_4$/NF

Typically, 0.238 g of $CoCl_2 \cdot 6H_2O$ and 0.242 g of $Na_2MoO_4 \cdot 2H_2O$ may be dissolved in 50 mL of de-ionized water, respectively. The mixture was then heated to 150 °C for one hour in a Teflon autoclave of 100 mL that contained Co_3O_4/NF. To prepare $CoMoO_4@Co_3O_4$/NF, the obtained sample was lastly annealed in air for two hours at 355 °C. For comparison, pure nickel foam devoid of Co_3O_4 is likewise added to the reactor and reacts in the same way to produce $CoMoO_4$/NF. The loading masses of Co_3O_4/NF, $CoMoO_4@Co_3O_4$/NF, and $CoMoO_4$/NF on the substrate are 1.8, 2.4, and 1.9 mg cm^{-2}, respectively. Figure 1 shows the $CoMoO_4@Co_3O_4$/NF preparation procedure.

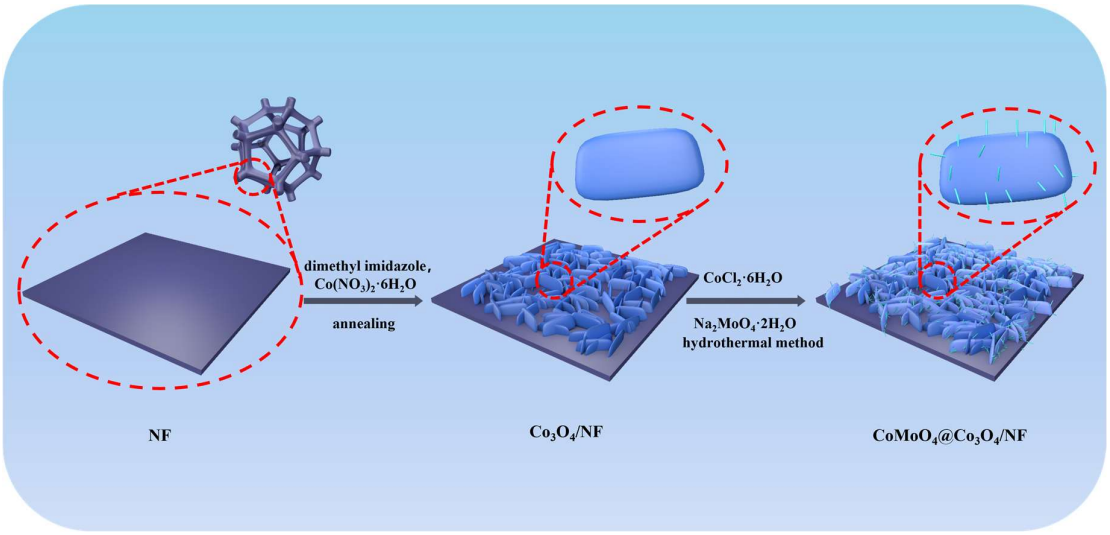

Fig. 1. Detailed schematic of the $CoMoO_4@Co_3O_4$/NF composites production process.

3. Results

The preparation process of $CoMoO_4@Co_3O_4$/NF hierarchical composite structure material is shown in Figure 2. In the beginning, Co_3O_4 was deposited on the exterior of nickel foam through solvent co-precipitation and subsequent annealing. Then, $CoMoO_4$ was grown on the Co_3O_4 surface using a hydrothermal method tailed by calcination. Thus, forming a $CoMoO_4@Co_3O_4$/NF hierarchical composite structure material. More reactive surface area is exposed in the layered composite structure when a $CoMoO_4$ layer forms on top of the outer layer of Co_3O_4. This layered composite structure promotes ion transport, leading to an enhanced participation of electrically active components in Faradaic redox reactions.

The materials' phase structure was investigated by XRD. Correspondingly, Figure 2a depicts three peaks corresponding to the CoMoO4 at the (001), (002), and (-311) crystal planes at an effective synthesis 13.2°, 26.5°, and 28.4°, respectively. Apparently, the peaks at 19.0°, 36.9°, 44.9°, 59.5°, and 65.4° correspond to Co3O4 (111), (311), (400), (511), and (440) planes, respectively, which is further evidence for the successful preparation of Co3O4. Therefore, the results of XRD confirmed that CoMoO4@Co3O4/NF had been prepared successfully with hierarchical composite structure material. Furthermore, the intensity of the Co_3O_4 diffraction peaks gradually decreases upon loading $CoMoO_4$, suggesting a decrease in crystallinity and an increase in the amorphous phase respectively. Additionally, the XRD pattern showed no peaks related to new impurities, indicating that the nickel foam surface does not contain any more impurity element.

In addition, nitrogen adsorption-desorption tests were conducted on Co_3O_4/NF, $CoMoO_4@Co_3O_4$/NF, and $CoMoO_4$/NF samples to probe their specific dimension and distribution of pores. Every sample displays H3-type hysteresis curves, as seen in Figure 2b, demonstrating the presence of a macroporous architecture. The specific surface area of $CoMoO_4@Co_3O_4$/NF (5.174 m^2 g^{-1}) was greater than that of Co_3O_4/NF (2.409 m^2 g^{-1}) and $CoMoO_4$/NF (3.227 m^2 g^{-1}) samples (Figure2b). In addition, CoMoO4@Co3O4/NF (Figure 2c) displayed more pores than Co_3O_4/NF and $CoMoO_4$/NF. The pore volume of $CoMoO_4@Co_3O_4$/NF (0.033 cc g^{-1}) was greater than that of Co_3O_4/NF (0.018 cc g^{-1}) and $CoMoO_4$/NF (0.022 cc g^{-1}). This allows for the rapid penetration of the electrolyte solution and allows for the inhalation of an extensive amount of active sites.

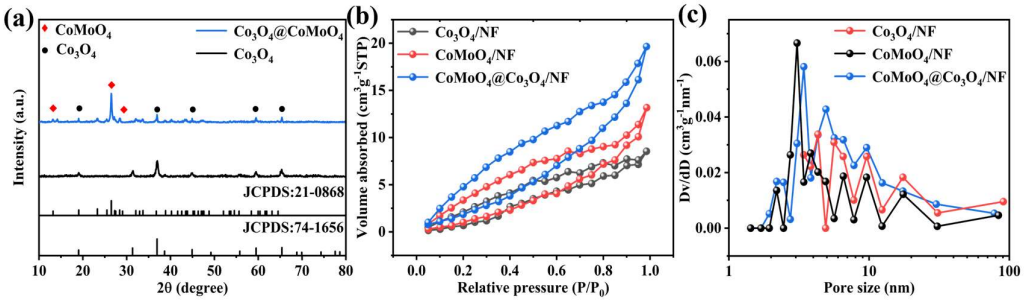

Fig. 2. (a) XRD pattern of Co3O4, Co3O4@CoMoO4 and CoMoO4; nitrogen adsorption/desorption isotherms as well as pore size distributions of Co3O4/NF, CoMoO4/NF and CoMoO4@Co3O4/NF samples are shown in (b) and (c), respectively.

XPS characterization was conducted to investigate the elements and their chemical states in CoMoO4@Co3O4/NF samples. The spectroscopic scan revealed the presence of Co, Mo, and O elements in $CoMoO_4$@Co_3O_4/NF, as displayed in Figure 3a. This is in good agreement with EDS spectroscopic analysis shown in Figure 5c-5e. In the high-resolution spectrum Co 2p, the presence of Co $2p_{3/2}$ at 780.9 eV, Co $2p_{1/2}$ at 796.6 eV, and two satellite peaks evidences the coexistence of Co^{3+} and Co^{2+} (Figure 3b). The complex spectral profile of Mo in Figure 3c is composed of two peaks at 231.9 eV and 235.0 eV, with a peak spacing of 3.1 eV. Those are ascribed to the Mo $3d_{5/2}$ and Mo $3d_{3/2}$ and reveal the presence of Mo^{6+} in $CoMoO_4$. Figure 3c displays Mo at its VI redox state with BEs at 231.9 eV and 235.0 eV conforming to Mo $3d_{5/2}$ and Mo $3d_{3/2}$, which is in good agreement with MoO_4^{2-}. Figure 3d shows the O1s spectra peak deconvoluted into three segments at 530.2 eV, 532.0 eV, and 533.4 eV, respectively. The former one is due to O2 oxide formed with the elements of Co and Mo, the mid peak is due to OH, and the latter due to C-O-C.

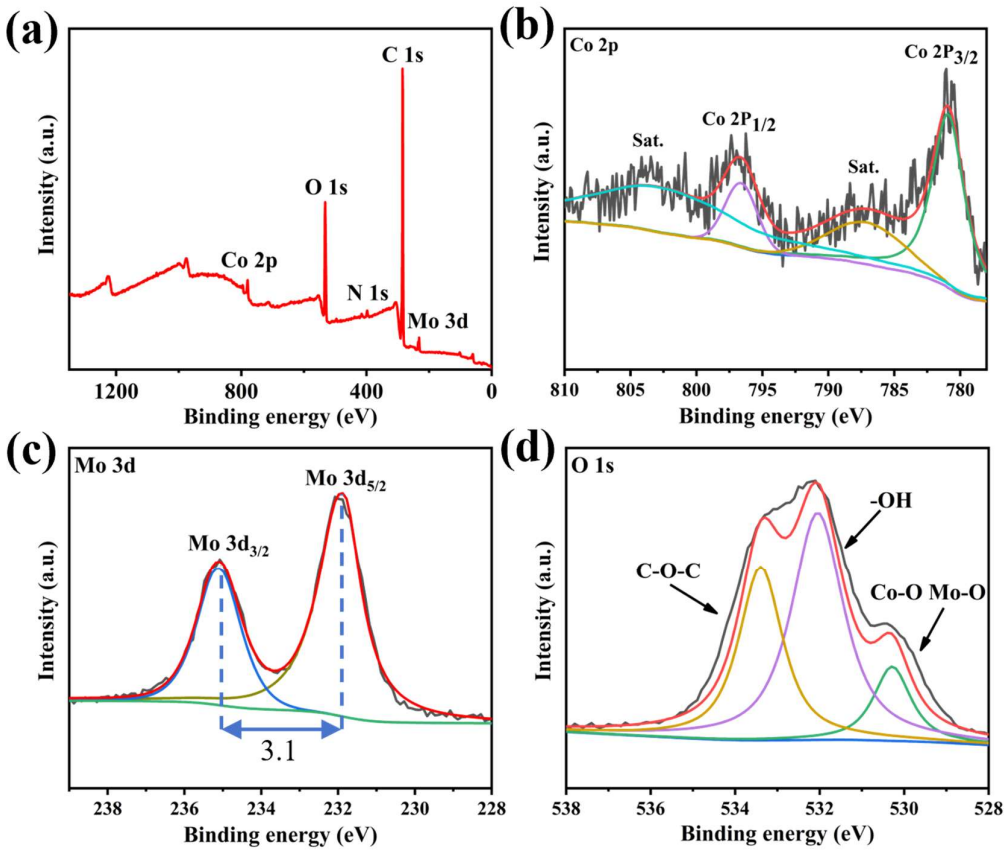

Fig. 3. (a) Higher-resolution spectra of the (b) Co 2p, (c) Mo 3d, and (d) O 1s; (XPS survey spectrum of Co-MoO4@Co3O4/NF).

SEM was used to examine the sample microstructures. As shown in Figure 4 (4a, 4b), Co_3O_4 was distributed relatively uniformly on nickel foam, presenting a sheet-like structure. Such a structure provides a substrate for the growth of $CoMoO_4$ with sufficient space and large surface area. However, as shown in Figure 4 (4c, 4d), pure $CoMoO_4$ nanorods grown on the nickel foam surface exhibited severe aggregation. In stark contrast, $CoMoO_4$ nanorods grown on the surface of Co_3O_4 nanosheets formed $CoMoO_4$@Co_3O_4/NF with hierarchical composite structure as shown in Figure 4 (4e, 4f). The hierarchical composite structure material prepared based on this principle exhibits a large specific surface area, with both outer and inner layers exposing more active sites. The collaborative effects among different components in the hierarchical composite structure are conducive to improving the electrode capacity. Likewise the electrode material's effectiveness during charge storage is enhanced by the electrolyte's complete contact with the cathode surface.

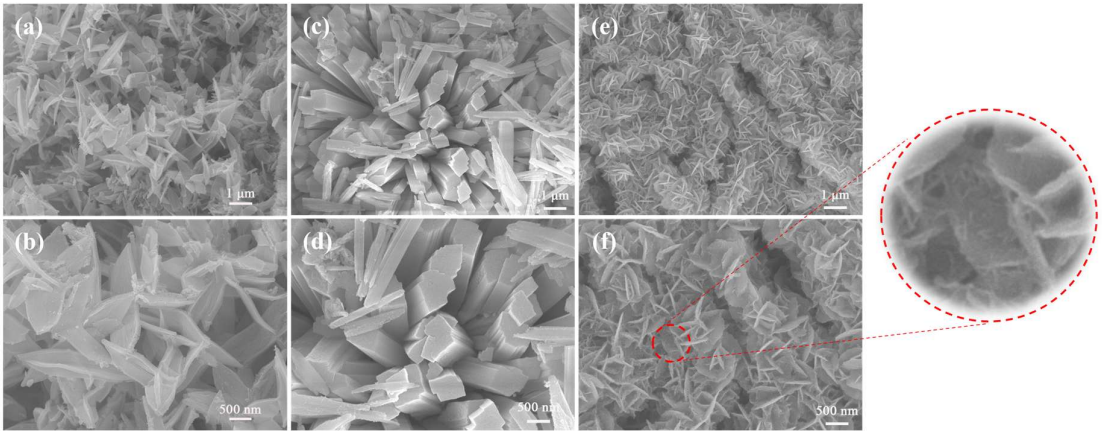

Fig. 4. SEM images; (a, b) Co3O4/NF, (c, d) CoMoO4/NF, and (e, f) CoMoO4@Co3O4/NF.

To further analyze the microstructure of $CoMoO_4$@Co_3O_4/NF, TEM and HRTEM examinations were conducted. As shown in Figure 5a, numerous nanorods are anchored onto nanosheets to form a hierarchical composite structure. As depicted in Figure (5d-5g), this hierarchical composite material is constituted by Co, O, Co, and Mo elements, indicating their successful synthesis. As demonstrated in Figure 5b, the lattice distance of 0.246 nm represents the (311) crystal plane of Co_3O_4, while Figure 5c shows that the lattice distance of 0.145 nm represents the (002) crystal plane of $CoMoO_4$. In conclusion, the hierarchical composite structure material $CoMoO_4$@Co_3O_4/NF has been successfully synthesized.

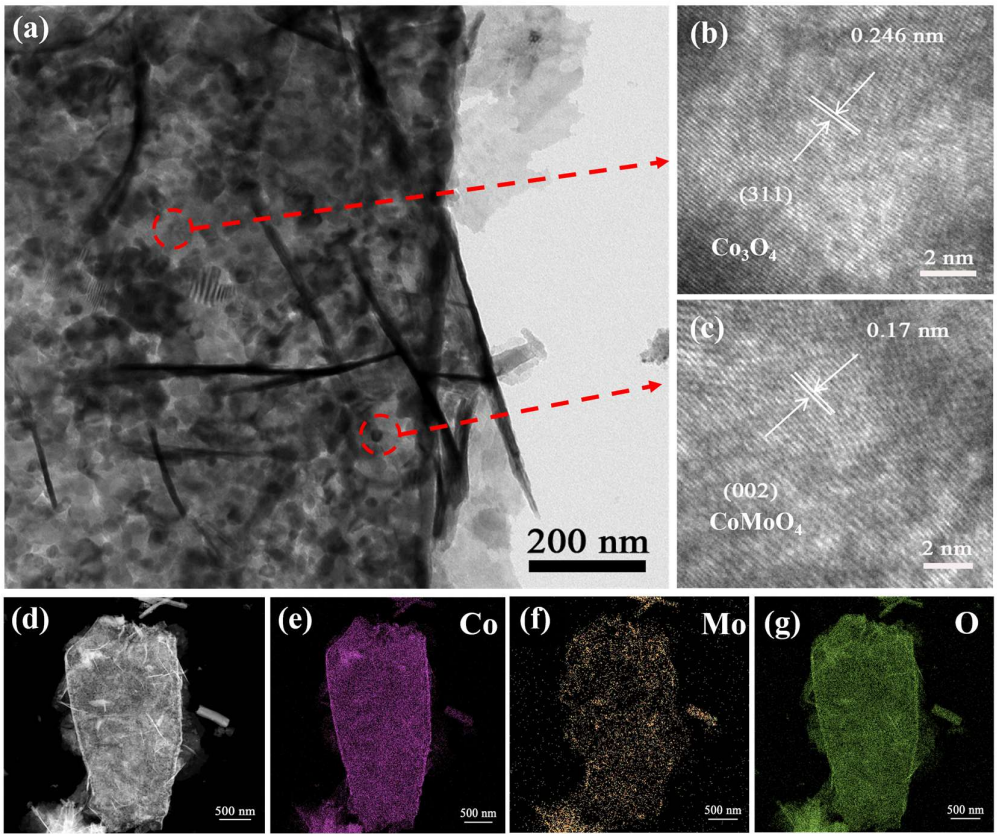

Fig. 5. (a) TEM images of CoMoO4@Co3O4/NF; (b, c) High-resolution TEM images of CoMoO4@Co3O4/NF; (d-g) corresponding elemental mapping images.

A tri-electrode setup in 3 M KOH was used to examine the electro-chemical characteristics of the composites. As seen in Figure S1, the foam exhibits a small CV curve area and a short GCD discharge time. The capacitance of nickel foam was only 0.005 F cm^{-2} at density of 1 mA cm^{-2}. Therefore, the contribution of nickel oxidation to the electrode capacitance can be neglected. The $CoMoO_4$@Co_3O_4/NF electrode clearly shows the biggest CV integration area at 15 mV s^{-1} (see Figure 6a), suggesting a greater individual capacitance in comparison to the other two electrodes. A specified 1 mA cm^{-2} voltage density was used for more measure the GCD curves (Figure 6b). $CoMoO_4$@Co_3O_4/NF demonstrated the longest discharge time, which confirmed its higher capacitance (specific). This can be ascribed to the hierarchical composite structure exposing more active sites that facilitate ion transport. Notably, a strong redox peak is observed in Figure 6c, which is credited to the reversible Faradaic-reactions between Co^{2+}/Co^{3+} and Mo $^{6+}$. With an enhance of scan rate, the peaks associated with oxidation and reduction shift slightly because of the rise in electrode diffusion resistance. Importantly, as shown in Figure 6d, each curve exhibits a distinct plateau, indicating a highly reversible redox reaction during the cycling process. The contributions of processes regulated by diffusion and capacitance were calculated using equation (6) to verify the charge storage mechanism of the $CoMoO_4$@Co_3O_4/NF electrode, as seen in Figure 6e. It was found that the anodic, and cathodic peaks had b values of 0.67 and 0.57, respectively. This suggests that both diffusion-controlled and capacitance processes have an impact on the charge storage process. The impact frequencies of processes that are governed by diffusion and capaciousness were computed to provide more insight into the charge storage mechanism (Figure 6f). The $CoMoO_4$@Co_3O_4/NF electrode showed a 96% diffusion-controlled contribution at a low scan rate of 1 mV s^{-1}, indicating that battery-type redox processes dominate in the electron transfer phase. The contribution ratio of processes controlled by diffusion reduces with increasing scan rate, but processes controlled by capacitance rise. This is mostly caused by a lack of redox reactions occurring at faster scan speeds as a result of quick electron/ion transfer. Capacitance-controlled activities can account for 82% of the total contribution when the scan rate is raised to 30 mV s^{-1}. EIS was further accompanied to analyze the electrochemical traits of all samples, as shown in Figure S2.c. Specific parameters are presented in Table S1. Compared with Co_3O_4/NF in the low-frequency area, the $CoMoO_4$@Co_3O_4/NF hierarchical composites ($CoMoO_4$/NF) show a slope, suggesting that Co_3O_4 properly lowers the electrode's ionic diffusion susceptibility. Additionally, in the high-frequency segment, the $CoMoO_4$@Co_3O_4/NF hierarchical composite material exhibits the smallest semicircle diameter, pointing to quick ion diffusion and efficient electron transfer. After 4,000 cycles at 10 mA cm^{-2} flow density, the $CoMoO_4$@Co_3O_4/NF hierarchical composite still retains 69% of its initial capacitance (Figure S2.d). Therefore, the above test indicates that $CoMoO_4$@Co_3O_4/NF possesses potential value for energy storage.

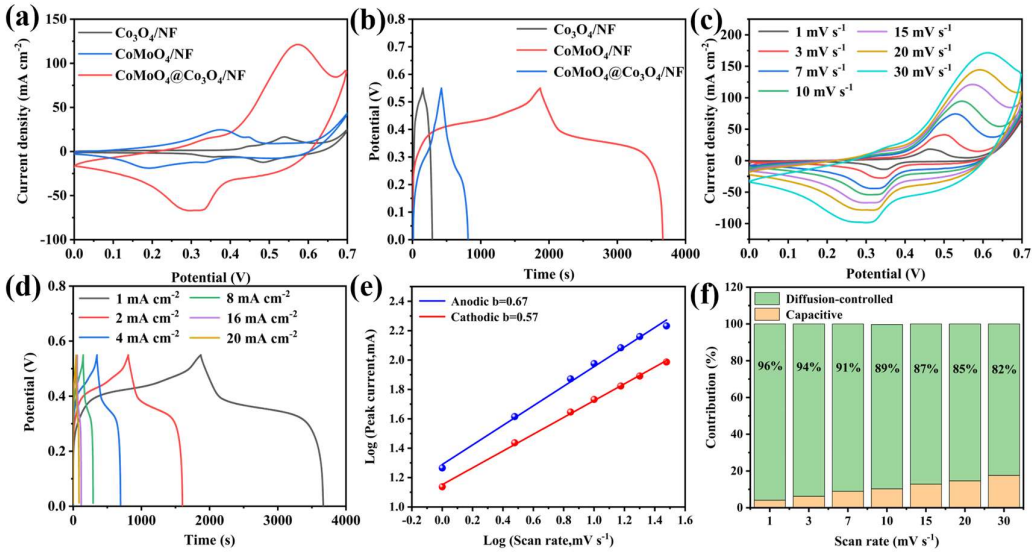

Fig. 6. (a) Co_3O_4/NF, $CoMoO_4$@Co_3O_4/NF, and $CoMoO_4$/NF CV curves at 15 mV s^{-1}; $CoMoO_4$@Co_3O_4/NF GCD curves at 1 mA cm^{-2}; $CoMoO_4$@Co_3O_4/NF CV curves at varying scan rates; $CoMoO_4$@Co_3O_4/NF GCD curves at varying current densities; (e) the b values for the anodic and cathodic peaks. (f) Contributions from capacity

Consequently, one piece of $CoMoO_4$@Co_3O_4/NF and one piece of AC were assembled as an anode and cathode, respectively, with KOH as the ion-conductive material, and its practical functionality was tested, as illustrated in Figure 7a. The CV curves of $CoMoO_4$@Co_3O_4/NF and AC at 15 mV s−1 show a maximum potential space, ranging from 0 to 0.7 V and −1 to 0 V, as shown in Figure S3.e. Consequently, an overall operating voltage window for $CoMoO_4$@Co_3O_4/NF//AC up to 1.7 V is expected. In addition, the practical voltage window can easily be extended up to 1.6 V as illustrated by the ASC CV curves at different voltage windows shown for Figure 7b. The shape of the CV curve in Fig. 7c evidences the exceptionality of the capacitance capability at various scan rates of this ASC, which gradually increased from 1 mV s−1 to 15 mV s−1 in the operating voltage window of 0-1.6 V. Figure 7d depicts that GCD curves developed at different current densities are more or less similar, which manifests the strong coulombic output with excellent electrochemical reversibility of the ASC. As shown in Figure S3.f, the electrochemical impedance spectroscopy (EIS) plots of the ASC before and after 6000 cycles are presented, and the specific parameters are listed in Table S2. Minor changes were observed in the region of low frequencies, indicating negligible variations in the capacitive behavior of the ASC. At higher frequencies, the estimated equivalent series resistance (Rs) was approximately 0.74 Ω, which was almost similar to that before the cycling. Surprisingly, the ASC achieved a preservation of capacitance 89% and a Coulombic utilization of 100% after 6000 cycles at a level of current density 10 mA cm^{-2} (Figure 7e). $CoMoO_4$@Co_3O_4/NF exhibits improved electrochemical performance when compared to the materials indicated in Table S3. Moreover, the improved porosity between the material used for the electrode and the salt solution, enhances the capacity of electrode to store vitality, is responsible for the rise in capacitance during the first cycle. The Ragone plot in Figure 7f. illustrates that $CoMoO_4$@Co_3O_4/NF //AC exhibits a significantly higher energy density of approximately 209.29 mWh cm^{-2} at a power density of 0.75 mW cm^{-2}. $CoMoO_4$@Co_3O_4/NF//AC has notable benefits over previously documented supercapacitors with asymmetry based on transition-metals compounds.

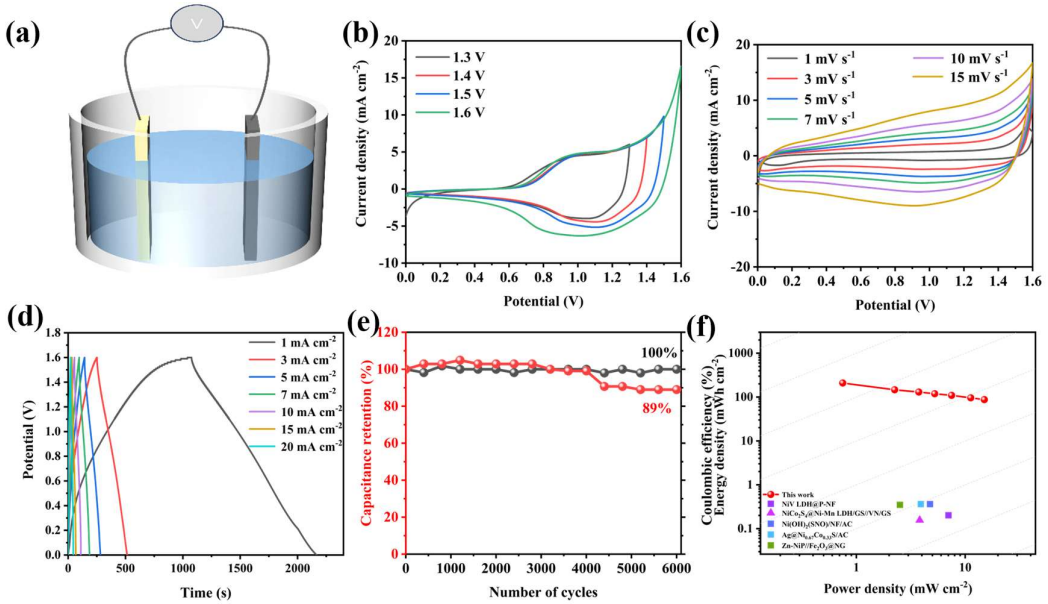

Fig. 7. (a) $CoMoO_4$@Co_3O_4/NF//AC test schematic. (b), different voltages (c), and different scan rates; (d) the ASC's specific-capacitance at various current density; (e) stability of ASC after 6,000 cycles at 10 mA cm^{-2};(f) the Ragone plot

4. Conclusions

The hierarchical composite $CoMoO_4$@Co_3O_4/NF was synthesized by co-precipitation, hydrothermal reaction, and calcination. In this composite, Co_3O_4 serves as the inner layer while $CoMoO_4$ forms the outer layer, and the collaborative effect between the inner and outer layers greatly augments the electrochemical output of the multicomponent electrode. Benefiting from the aforementioned advantages, the $CoMoO_4$@Co_3O_4/NF hierarchical composite structure material exhibits robust electrochemical performance and durability of cycling. The $CoMoO_4$@Co_3O_4/NF electrode that was created has an extraordinary specific-capacitance of 3.385 F cm^{-2}. This is at a current density of 1 mA cm^{-2}. The assembled $CoMoO_4$@Co_3O_4/NF//AC ASC exhibits excellent specific-capacitance (0.669 F cm^{-2} at 1 mA cm^{-2}) and impressive energy density (209.29 mWh cm^{-2}), while ensuring a consistent cycling stability with 89% maintenance of capacity after 6000 cycles at 10 mA cm^{-2}. Therefore, the electrode assembled with $CoMoO_4$@Co_3O_4/NF hierarchical composite material holds tremendous potential for application in supercapacitors.

References

[1] Li, X., Chen, X., Yi, Z., Zhou, Z., Tang, Y., & Yi, Y. (2019). Fabriction of ZnO nanorods with strong UV absorption and different hydrophobicity on foamed nickel under different hydrothermal conditions. Micromachines, 10(3), 164.

[2] Siwek, K. I., Eugénio, S., Santos, D. M. F., Silva, M. T., & Montemor, M. F. (2019). 3D nickel foams with controlled morphologies for hydrogen evolution reaction in highly alkaline media. International journal of hydrogen energy, 44(3), 1701-1709.

[3] Gao, H., Wang, Y., Zhou, S., Song, S., Tian, X., Li, W., ... & Zang, J. (2021). Nickel-cobalt phosphate nanoparticles wrapped in nitrogen-doped carbon loading on partially phosphatized foamed nickel as efficient electrocatalyst for water splitting. Chemical Engineering Journal, 426, 130854.

[4] Bu, X., Wei, R., Cai, Z., Quan, Q., Zhang, H., Wang, W., ... & Ho, J. C. (2021). More than physical support: The effect of nickel foam corrosion on electrocatalytic performance. Applied Surface Science, 538, 147977.

[5] Zhao, B., Zheng, P., Yang, Y., Sha, H., Cao, S., Wang, G., & Zhang, Y. (2022). Enhanced anaerobic digestion under medium temperature conditions: Augmentation effect of magnetic field and composites formed by titanium dioxide on the foamed nickel. Energy, 257, 124791.

[6] Yu, S. Y., Mei, L. P., Xu, Y. T., Xue, T. Y., Fan, G. C., Han, D. M., ... & Zhao, W. W. (2019). Liposome-mediated in situ formation of AgI/Ag/BiOI Z-scheme heterojunction on foamed nickel electrode: a proof-of-concept study for cathodic liposomal photoelectrochemical bioanalysis. Analytical chemistry, 91(6), 3800-3804.

[7] Yan, J. Y., Cao, C. Y., Cao, G. P., Pan, S. F., Lv, H., & Saeed, A. M. (2024). Mechanism of NCNTs Growth on Foamed Nickel and Thus-Prepared PS Hydrogenation High-Performance Carrier NCNTs@ FN. Langmuir, 40(13), 6786-6805.

[8] Koshy, S. S., Rath, J., & Kiani, A. (2024). Fabrication of binder-less metal electrodes for electrochemical water splitting–A review. Heliyon.

[9] Nagaraju, G., Cha, S. M., Sekhar, S. C., & Yu, J. S. (2017). Metallic layered polyester fabric enabled nickel selenide nanostructures as highly conductive and binderless electrode with superior energy storage performance. Advanced Energy Materials, 7(4), 1601362.

[10] Kang, Y., Deng, C., Chen, Y., Liu, X., Liang, Z., Li, T., ... & Zhao, Y. (2020). Binder-free electrodes and their application for Li-ion batteries. Nanoscale research letters, 15, 1-19.

[11] Berenguer, R., García-Mateos, F. J., Ruiz-Rosas, R., Cazorla-Amorós, D., Morallón, E., Rodríguez-Mirasol, J., & Cordero, T. (2016). Biomass-derived binderless fibrous carbon electrodes for ultrafast energy storage. Green Chemistry, 18(6), 1506-1515.

[12] Lacey, S. D., Walsh, E. D., Hitz, E., Dai, J., Connell, J. W., Hu, L., & Lin, Y. (2017). Highly compressible, binderless and ultrathick holey graphene-based electrode architectures. Nano Energy, 31, 386-392.

[13] Komoda, M., & Nishina, Y. (2022). Fabrication of binderless electrodes via non-destructive electrochemical oxidation/reduction of graphite sheets using BF4 salts. Electrochimica Acta, 430, 141087.

[14] Lee, H., Bak, C., Lim, M., An, H., Byun, S., Lee, Y. M., & Lee, H. (2023). Preplanting Nanosilica into Binderless Battery Electrodes for High-Performance Li-Ion Batteries. ACS Applied Nano Materials, 6(4), 3128-3137.

[15] Kim, T. H., Veerasubramani, G. K., & Kim, S. J. (2018). Hierarchical porous flower-like nickel cobaltite nanosheets as a binder-less electrode for supercapacitor application with ultra-high capacitance. Journal of industrial and engineering chemistry, 61, 181-187.

[16] Orlova, T. S., Shpeizman, V. V., Glebova, N. V., Nechitailov, A., Spitsyn, A. A., Ponomarev, D. A., ... & Ramirez-Rico, J. (2018). Environmentally friendly monolithic highly-porous biocarbons as binder-free supercapacitor electrodes. Reviews on Advanced Materials Science, 55(1), 50-60.

[17] Talebi, M., Ahadian, M. M., Shahrokhian, S., & Amini, M. K. (2021). Fabrication of porous polyphosphate carbon composite on nickel foam as an efficient binder-less electrode for symmetric capacitive deionization. Separation and Purification Technology, 276, 119427.

[18] Cheng, Y., Wang, X., Zhang, D., Qiao, X., Zhao, H., Chang, L., ... & Yang, S. (2022). High-capacity binderless supercapacitor electrode obtained from sulfidation large interlayer spacing of NiMn-LDH. Electrochimica Acta, 429, 141039.

[19] Brambilla, N. (2020, November). Introduction to Neocarbonix: Binderless Electrodes for Lithium-Ion Batteries. In Electrochemical Society Meeting Abstracts prime2020 (No. 2, pp. 337-337). The Electrochemical Society, Inc..

[20] Shaikh, S., & Rabinal, M. K. (2022). Facile one-step growth of nickel sulfide nano-architecture as binder less electrodes for efficient supercapacitor applications. Materials Science in Semiconductor Processing,

142, 106524.

[21] Parveen, N. (2024). Resent Development of Binder‐Free Electrodes of Transition Metal Oxides and Nanohybrids for High Performance Supercapacitors–A Review. The Chemical Record, 24(1), e202300065.

[22] Pang, M., He, W., Song, Z., Zhang, R., Jiang, S., Mao, M., ... & Zhao, J. (2023). Engineering hierarchical honeycomb-wall-like MgP4O11/CoP nanosheets as advanced binder-less electrode for supercapacitors. Colloids and Surfaces A: Physicochemical and Engineering Aspects, 674, 131927.